JOINT EUROPEAN TORUS

JET–P(91)06

M.A. Kovanen, R. Reichle, E. Lazzaro, D.D.R. Summers, T. Taylor
and JET Team

Modelling of the Observed Particle and Heat Fluxes in the X-Point Region at JET

"This document contains JET information in a form not yet suitable for publication. The report has been prepared primarily for discussion and information within the JET Project and the Associations. It must not be quoted in publications or in Abstract Journals. External distribution requires approval from the Publications Officer, JET Joint Undertaking, Abingdon, Oxon, OX14 3EA, UK".

"Enquiries about Copyright and reproduction should be addressed to the Publications Officer, EFDA, Culham Science Centre, Abingdon, Oxon, OX14 3DB, UK."

The contents of this preprint and all other JET EFDA Preprints and Conference Papers are available to view online free at www.iop.org/Jet. This site has full search facilities and e-mail alert options. The diagrams contained within the PDFs on this site are hyperlinked from the year 1996 onwards.

Modelling of the Observed Particle and Heat Fluxes in the X-Point Region at JET

M.A. Kovanen[1], R. Reichle, E. Lazzaro[2], D.D.R. Summers, T. Taylor[3]
and JET Team*

JET-Joint Undertaking, Culham Science Centre, OX14 3DB, Abingdon, UK

[1]Lappeenranta University of Technology, Finland and National Research Council for Technology, The Academy of Finland.
[2]Present Address: Institute for Plasmaphysics, Milan, Italy.
[3]Present Address: General Atomics Incorporated, San Diego, USA.
** See Appendix 1*

Preprint of Paper to be submitted for publication in
Nuclear Fusion

Modelling of the Observed Particle and Heat Fluxes in the X-Point Region at JET

M.A. Kovanen[1], R. Reichle, E. Lazzaro[2],
D.D.R. Summers, T. Taylor[3]

JET Joint Undertaking, Abingdon, Oxon. OX14 3EA, U.K.

Abstract

Particle and heat fluxes at the upper X-point region in JET ohmic and auxiliary heated discharges are deduced from the experimental CCD camera and magnetic measurements. Modelling of the particle and heat transport processes at the edge of the plasma with Monte Carlo orbit following calculations agree well with the observations. The importance of the finite orbit effects in low collisionality plasmas is assessed. It is found that the convection by plasma ions plays a very important role in the heat transport from the plasma to the wall.

1. Introduction

A substantial improvement in the plasma confinement properties, the H-mode, has been obtained in several experiments (ASDEX, DIII-D, PDX) using a poloidal divertor configuration. In JET a magnetic separatrix is produced without a divertor chamber or a large vacuum region giving, however, similar plasma behaviour to that in the divertor tokamaks [1].

The presence of the X-point strongly affects the heat and particle flows from the plasma to the wall. These fluxes, which can be observed experimentally with CCD cameras and Langmuir probes, have conventionally been regarded as heat conduction by electrons [2]. In JET two CCD cameras are used to measure the energy and particle fluxes at the wall in the upper X-point region. The discrete X-point wall tiles are curved in the toroidal direction and,

---

[1]Lappeenranta University of Technology, Finland and National Research Council for Technology, The Academy of Finland.
[2] Present address: Institute for Plasmaphysics, Milan, Italy
[3] Present address:General Atomics Incorporated, San Diego, U.S.A.

thus, particles striking the wall on the opposite sides of the apex of the curvature correspond to flows along the magnetic field lines from different directions. The interpretation has been that the strike zones are the footprints of the heat flow along the magnetic separatrix [3]. This, however, often does not coincide with the magnetic measurements of the separatrix and X-point location (Fig. 1). Two or sometimes three radially well separated zones of intense light are observed even when the upper magnetic X-point is found to be just above the wall tiles.

The electrons flow along the field lines. Due to the finite width of the drift orbits, scattering of ions in velocity space to loss regions will take them to orbits which intersect the wall on or outside the separatrix. The distance between the separatrix and the impact points depends on the drift terms of the orbits. In the region of low poloidal magnetic field strength, B_ϕ, the magnetic and diamagnetic drifts dominate over the parallel one. Thus, in the X-point region the finite orbit width can be very large and the deposition points a substantial distance away from the separatrix.

Ion transport through the tokamak separatrix was considered by HINTON and CHU by obtaining the ion distribution function from the orbit-averaged drift kinetic equation with a variational principle [4]. The work was then extended to study the H-mode transition which also included the collision dominated regime [5]. The collisional transport of electrons and ions in the scrape-off layer of a diverted tokamak plasma was investigated by HINTON and STAEBLER [6]. In this work the strength of the plasma pinch effect was computed using a simple model and DIII-D data. In our study kinetic simulation by the orbit following Monte-Carlo code HECTOR [7] is used, to explain the observed heat and particle flows in the X-point region at JET. The structure of this paper is as follows. In Section 2 the method for measuring the heat flux patterns in JET is described and the experimental observations presented. The magnetic calculations of the X-point location are described in Section 3. In Section 4 simple orbit calculation is used to assess the orbit effects on the particle and heat fluxes on the wall. The numerical model is described in Section 5 and the results which are shown to agree well with the observations are presented and discussed in Section 6. Finally, Section 7 contains the summary.

2. Experimental Heat Flux Measurements

2.1 Diagnostic Methods

To measure the spatially resolved temperatures and particle fluxes at the target tiles in the upper X-point region charge coupled device (CCD) cameras with narrow band interference filters, video recorders and a digital video analysis system were used at 3 of the 32 bands of target tiles. Spatially integrated measurements with a wide dynamic range were obtained with an optical multichannel analyser (OMA) [8]. One of the CCD cameras was equipped with a filter changer for H_α, C_I (909.5nm), C_{II} (515.4nm) and C_{III} (464.7nm) intensity measurements. The other camera used a 1mm filter for the temperature measurement. The OMA system shared the view of this camera by means of an optical beam splitter. The spectral lines recorded with the OMA included H_α, C_{II} (657.8nm) and Be_{II} (463.0nm).

As the discrete target tiles are curved in the toroidal direction the infrared images used for the temperature measurements show the strike zones of particles on the target plates as localised bright spots (Fig. 2). The maximum of the particle flux intensity derived from the spatially resolved H_α and carbon line emission coincides with these strike zone positions.

A more detailed description of the diagnostic methods for the heat flux measurements in JET can be found in [9].

2.2 Measurements

Two opposite particle flows, of which the outer one on the electron drift side has higher heat flux than the inner one on the ion drift side, are seen during ohmic discharges (Fig. 2). During auxiliary heating with up to 20MW of neutral beam injection or up to 18MW of ion cyclotron resonance heating, three bright zones are often observed when either the H_α or the C_{III} filter are used but only two of the zones show significant thermal loads with the 1μm filter (Fig. 3). In the purely ohmic phase there is an outer zone (A) on the electron drift side and a weak inner zone (C) on the ion drift side. When the heating is applied, the intensity of zone A increases and a third bright strike zone (B) appears between zones A and C on the ion drift side while the intensity of zone C remains the same or decreases. The examination of all 32 bands of tiles clearly showed erosion at strike zone positions A and B [10]. However, significant

erosion at zone B was found only on 8 bands of tiles while the erosion at zone A was on 29 bands. Thus, assuming that the alignment accuracy of the tiles at the two zones is the same, there is an indication that the particle impact angle with the wall is smaller at zone B than at zone A. Dividing the flux of particles by the power deposited onto the target tiles gives higher particle mean energy at zone B than at zone A. Although a larger power flux was observed at strike zone B, because it occurred at fewer bands, the total integrated power around the torus is smaller at zone B than at zone A.

Figure 4 shows the temporal behaviour of the temperature, the power as derived from that temperature, and the deuterium and carbon fluxes at the centres of strike zones during auxiliary heating. We see the temperature of strike zone A rise earlier than that of zone B which, however, will later increase rapidly and exceed the temperature at zone A. Furthermore, there is a delay of 0.2sec for strike zone A and 0.3sec for strike zone B between the onset of the NBI heating and the detection of the temperature rise at the target tiles. The carbon influx, which is associated with a high tile surface temperature, is dominated by the flux originating from strike zone B and a carbon bloom via thermal sublimation occurs when the temperature at strike zone B reaches 2400°C. The deuterium flux signal is constant during the rise of the carbon influx.

3. Magnetics

The magnetic equilibrium is obtained with the reconstruction code IDENTC [11]. The code solves the Grad-Shafranov equation for the plasma free boundary equilibrium using as the boundary condition the external magnetic flux measurements and parameterised representations of the toroidal current density and pressure profiles. Free parameters are adjusted to fit optimally the magnetic measurements which also include the tangential magnetic field. The magnetic detection of the X-point from this reconstruction may suffer from uncertainties due to systematic errors in the magnetic flux signals with a typical fitting error of 4% in X-point discharges. The calculation is done with a Finite Element algorithm supplemented by an accurate interpolation. Furthermore, the location of the X-point is essentially dictated by the ratio of the shaping current (PF2) to the plasma current and is necessarily along the straight line

joining the plasma (current) axis and the coil axis. Modifications of the location require relatively large variations of the plasma or shaping currents and cannot be brought about by transient events involving small quantities of energy. In addition, detection of the X-point involving only a local expansion and using the poloidal magnetic field measurements in the vicinity of the X-point gives similar results to those of the reconstruction code [12].

4. Numerical Model

The particle orbit drifts become an important consideration in the heat flux on the target tiles when the ratio of the drift to scrape off widths, $\delta_{drift}/\delta_{S.O.L.}$, approaches unity. In most JET plasmas $\delta_{S.O.L.}$ is of the order of a few millimetres to a centimetre and

$$\delta_{drift} = v_{drift} \frac{\ell_{\|}}{v_{\|}}, \tag{1}$$

where $v_{\|}$ is the particle velocity along the magnetic field line and $\ell_{\|}$ is the length of the field line from the plasma to the tiles. The curvature and grad B drifts can be estimated from

$$\delta_{drift}^{e,i} \sim \frac{C_{e,i} T_{e,i}^{1/2} \ell_{\|}}{RB}, \tag{2}$$

where the subscripts e and i refer to electrons and ions, respectively, $\ell_{\|}/(RB) \sim 1\text{-}2$, $C_e \sim 5 \times 10^{-6}$ and $C_i \sim 2 \times 10^{-4}$. It is clear that orbits of ions above a few hundred eV can be important.

Usually the orbit topology is included in the heat flux calculations by mapping the source function on the wall. This is done by solving the interaction points of the drift orbits with the wall. In this method of treatment only prompt particle losses are included, and it is relevant solely for thermonuclear reaction products. This plays an insignificant role in the heat flux from the JET D-plasmas. Furthermore, although the heat flux profile from the wall is flatter than that from the fluid model, the position of the heat zones is the same. For example, if we have the X-point outside the vessel, the co and counter streaming prompt particle losses would produce a heat zone at a single point where the wall is tangential to the last closed flux surface, contradicting the experimental evidence of at least two strike zones. Thus, the inclusion of the finite width of the particle orbits can not on its own describe the heat flux patterns on the wall. In order to rectify the situation, an alternative solution procedure is

required. How quickly each particle is lost to the wall after scattering to the loss cone depends on the orbit topology. As the collisional processes attempt to maintain an isotropic distribution in velocity space, the steady state flow of particles into the loss cone becomes non uniformly distributed. It is then the distribution of delayed losses which determines the heat flux patterns on the wall.

In our study the heat flux patterns in the JET X-point region are calculated with the Monte-Carlo orbit following code HECTOR in which a proper treatment of the delayed losses is included. The code follows the guiding centres of the charged particles in axisymmetric tokamak plasma using the constants of motion (C.O.M.) method. For a collisionless particle trajectory this method conserves the particle energy E, the magnetic momentum and the toroidal canonical angular momentum, respectively,

$$\mu = \frac{1}{2} m v_{\perp}^2 / B \tag{3}$$

$$P_{\phi} = mRv_{\phi} - Ze\psi,$$

where m and Ze are the particle mass and charge, respectively, R is the major radius, ψ is the poloidal flux function, $v_{\perp}$ is the perpendicular velocity component, and the toroidal component $v_{\phi} = v_{\parallel} B_{\phi}/B$. The steady state flow of source particles into the loss cone is provided by the Coulomb collision processes of dynamical friction, pitch angle scattering and energy diffusion, which are included by changing the (P_{ϕ},μ,E) coordinates after each integration time step. The usual feature of cumulative errors in orbit following procedures introduced by both the orbit integration itself and the inclusion of scattering processes is absent in the model.

The magnetic equilibrium is obtained from the IDENTC code, and the plasma density and temperature profiles are read from JET shot data banks. Although an accurate description of the JET wall is used, the curvature of the target tiles in the toroidal direction is not included. However, the direction of the heat flow can in the model be determined from the sign of $v_{\parallel}$.

The total number of test particles has to be limited to obtain a reasonable computing time. Thus, to improve the accuracy of the wall load calculations the test particle source is initially concentrated in a thin layer just inside the separatrix. The source layer of 10-15 cm on the mid-plane in the ohmic discharges and twice this width in auxiliary heated plasmas is

sufficient to provide a continuous, undisturbed flow of particles to the loss cone at the very edge of the plasma. A reasonably long orbit following time is needed to obtain a statistically sufficient number of test particles intersecting the wall, and to exclude the transition period during which the S.O.L. is created by the neoclassical transport processes. Initially, particles have Maxwellian velocity distribution and are isotropic in velocity space. Since particles produced in different regions of phase space are simply connected through the unique set of (P_ϕ,μ,E) coordinates, all particles produced in a particular orbit connecting different regions of phase space are equivalent. 2000 of these bounce averaged test particles are followed, taking 15-20 min CPU time on IBM-3090 - 300J.

5. Results and Discussion

5.1 X-Point Location Effects

In ohmic discharges the simulation produced two strike zones, the position and the relative intensities of which agree well with the CCD camera observations (# 19414, t = 49.5 s) (Fig. 5). Furthermore, the direction of the heat flows producing the strike zones on the opposite sides of the target tiles is reproduced by the simulation. These results contradict the earlier interpretations of the X-point position from the heat flux measurements and show that the calculated X-point location does not misrepresent the experiments. The response of the strike zone positions to the horizontal sweep of the X-point (# 19414) is also seen in the simulation (Fig. 6).

While the effect of the radial changes in the X-point location is to produce similar changes in the strike zone positions, a vertical sweep of the X-point produced significant differences in the positions of the strike zones, particularly when comparing cases of X-point being inside and outside the vessel. In Fig. 7 we demonstrate the effect of the vertical sweep of the X-point on the heat flux pattern by changing the position of the vessel wall in a fixed magnetic field configuration (# 19414, t = 49.5s). Due to uncertainty in the relative values of the plasma edge parameters in the different X-point configurations represented here, the total heat flux was kept constant. In addition, the different profile effects in the H- and the L-modes were not included. When the X-point is well inside the plasma only those particles which

scatter outside the separatrix can be lost on the wall and the heat flux zones are separated by a considerable distance. The peak of the inner strike zone is radially slightly shifted inwards from the point where the separatrix intersects the wall and the outer strike zone is shifted outwards in a similar way, a feature which is absent in the fluid model. Moving the X-point outside the vessel forms a limiter type plasma in which the separation of the zones is shorter than when the X-point is inside the vessel. The strike zones have a minimum, non-zero, distance. The position of the X-point for the minimum separation depends not only on the profile effects but also on the expansion of the flux surfaces and, thus, it may occur when the X-point is a few centimeters inside the vessel.

5.2 Auxiliary Heated Discharges

During auxiliary heating when three zones of intense light are observed the middle zone (B), close to the radial X-point location, appears some time after heating is switched on. Furthermore, it has been shown that most of the H-mode discharges in JET during the 1989 campaign have a limiter type X-point plasma [12]. As such a discharge would be expected to produce only two strike zones the question arises as to whether strike zone B would be associated with the high energy ICRF heated minority ions or with the fast NBI particles. ICRF wave fields are focused in JET in a small region in the centre of the discharge. Although MeV range particles are produced, the velocity distribution is highly anisotropic with a significant fraction of minority ions trapped in the toroidal magnetic field making losses of these particles very small [13]. The neutral beam injection in JET produces trapped particle orbits of which some at the edge of the plasma could intersect the wall in the X-point region. However, the distribution in pitch angle required for these losses represents only a fraction of the total distribution for the beams. Furthermore, the source strength for the fast ions at the edge of the plasma calculated with the PENCIL code [14] is far too weak to correspond with the observed heat flux and unrealistically strong blocking of the beam power would have to occur in the S.O.L.

As the fast NBI particles or ICRF heated minority ions are not the course of strike zone B, let us now examine the considerable experimental evidence [15] which shows that during

auxiliary heating the plasma edge ion temperature increases to 1-3 keV at the separatrix from 100-200 eV in the ohmic phase. This effect was simulated in a typical limiter type X-point discharge (# 20998, t = 51.0sec) by varying the ion temperature while keeping the other plasma parameters and the magnetic field configuration the same and allowing the total heat flux to vary. We see in Fig. 8 that the radial position of the X-point is substantially closer to the inner strike zone than to the outer one. This is a geometrical effect arising from the radial position of the X-point which is at the inboard side of the current centre. The distance of both of the strike zones from the tangency point appears to be the same. The effect is seen more clearly in limiter type X-point discharges than in the ones where the X-point is inside the vessel. We also see that the positions of the strike zones during the ion temperature scan did not change. As the T_i is increased, particles deposit their energy radially further out from the X-point location. However, as the loss region in the plasma expands radially at the same time, more particles from further in are lost near the tangency point. Thus, the strike zones will become wider but the centres do not move. Because of this overlapping of orbits of particles with different energy and the radial position of the source, the distribution of the mean particle energy within the strike zones is reasonably flat.

When the ion temperature is increased the heat flux on the outer strike zone increases but at a slower rate than T_i. Fig. 9 shows that the particle flux on the outer zone increases when the ion temperature is raised from 100eV to 250eV but for higher temperatures it is reduced. It appears that at a low temperature the collision frequency stays higher than the loss rate in spite of some increase in temperature. However, when the temperature goes further up the collision frequency decreases to such an extent that it is not possible to fill the whole loss cone which results in a reduced particle flux and in the creation of an unisotropic velocity distribution at the edge of the plasma. At the inner strike zone on the other hand, both the heat and the particle fluxes increase with the ion temperature. In Table I we see that the mean energy of the striking particles is higher at the outer zone, at $T_i(\psi_n = 1.0) = 100$eV but for ion temperatures >250eV it is higher at the inner zone. Thus, a source of high energy particles gives a larger rise to the inner particle and heat fluxes than to those at the outer zone during auxiliary heating. This source is illustrated in Fig. 10 in which the loss cone orbits for particles

at E_1 and E_2 energies ($E_1 < E_2$) are shown at given source points (A-D). The vertical asymmetry of the target positions represents a typical JET X-point discharge. In the heated plasma ($E = E_2$) the inner and outer strike zones receive particles from source points A and B, respectively. As particles from point B can reflect back in the magnetic field, a lower load will occur at the outer zone. Furthermore, a low collision frequency is needed to charge some of the otherwise confined particles from source point C to trapped ones which can then reach the wall on the high field side. Thus, the increase of the finite orbit width with the ion temperature leads to a higher mean energy and heat flux at the inner strike zone than at the outer one. The magnitude of the wall load at the bottom of the vessel depends on the relative distance of the lower and the upper X-points from the wall and not on the direction of the $\vec{B}\times\nabla B$ drift, as the particle orbits are symmetrical in the vertical direction in the magnetic coordinates.

It is clear that the simulated inner and outer strike zones correspond to the experimental zones B and A, respectively. Our simulation also shows that the strike zone B exists, though weak, even in the ohmic phase, in which the heat flux to zone B is very weak and likely to be below the detection limit of the CCD camera. When we take into account the time it takes to heat the edge plasma after applying auxiliary heating, similar temporal behaviour in the intensity of this strike zone, as observed with the CCD cameras, would be indicated.

The high C_{III} intensity in zone C (Fig. 3) is associated with the low ionization/excitation ratio for low energy particles and so spectral emission near zone C exceeds that from zone B which is not observed until the surface is significantly heated. Furthermore, no thermal radiation is observed at zone C. Thus, although there must be a high particle flux to zone C, the heat flux has to be very small. A likely source of these low energy ions is the influx from the wall. The effect of this influx was simulated by adding a simple particle source with the density and temperature profiles in the form of $e^{-x/\alpha}$, where x is the distance from the separatrix, and $\alpha \sim$ 1cm, and assuming T_i (x = 0) = 1 keV and T_{influx} (x = 0) = 10 eV. In Fig. 11 we see that although the peak of the inner heat flux zone (corresponding to zone B) is not changed, the peak of the particle flux is slightly moved inwards. This indicates that the influx of low energy particles could load the wall slightly off strike zone B. Due to the measurement technique two separate zones C and B are then observed. The influx zone on the

outboard side was widely spread due to the geometry of the wall and the magnetic topology, and is not verified experimentally as the load area reaches out of the CCD camera view.

The CCD camera measurements and the results from the Monte Carlo modelling have ruled out a significant additional heat flow out of plasma due to the conduction by electrons which would have produced different strike zones from those experimentally observed. However, there is a situation where conduction may emerge. When the temperature of the carbon surface reaches 2200°C, the thermionic electron emission can become strong enough to destroy the sheath potential in front of the target tile allowing an electron flow onto the tile. An indication of this is that the energy per particle hitting the strike zone calculated from the measured heat flux is higher than that found by doppler broadening spectroscopy . Thus, convection by plasma ions may create a channel for conduction in the strike zones.

6. Summary

Particle and heat fluxes at the upper X-point region in JET have been deduced from the experimental measurements. The temperature and particle fluxes on the upper target tiles were measured with two CCD cameras. In the ohmic phase two clearly separated heat flux regions, strike zones, appear on the wall. During the auxiliary heating three bright zones are seen of which the middle and the outer ones show very high intensity while the inner one is weak. Whereas the fluid model is inadequate to describe the heat flux pattern on the X-point tiles, the Monte Carlo modelling of the particle and heat transport processes agrees well with the experimental observations for the direction of the heat flows, the positions and the relative intensities of the strike zones, and allowing the time for the plasma edge to heat up during the auxiliary heating, also, for the temporal behaviour of the strike zones. This agreement shows that the X-point positions from the reconstruction or the local expansion codes represent the experiments correctly. The heat flux patterns show that the heat transport from the plasma to the X-point tiles is dominated by the convection by plasma ions. However, convection may induce a local channel in the strike zones for conduction by electrons.

Acknowledgement

It is a pleasure to acknowledge J. Callen for useful discussions, and M. Keilhacker for useful comments on the manuscript. We also thank D. Muir for calculating the neutral beam deposition profiles, M. Pick for supplying us the tile erosion data, and M Stamp for supplying the OMA data.

M.A. Kovanen wants to thank JET Theory Division for hospitality, and the Finnish Cultural Foundation for financial support.

References

[1] TANGA, A., BEHRINGER, K.H., COSTLEY, A.E., et al., Nucl. Fusion 27 (1987) 1877.

[2] BRAAMS, B.J., HARBOUR, P.J., HARRISON, M.F.A., HOTSTON, E.S., MORGAN, J.G., J. Nucl. Mater. 121 (1984) 75.

[3] HARBOUR, P.J., SUMMERS, D.D.R., CLEMENT, S., COAD, J.P., DE KOCK, L., EHRENBERG, J., J. Nucl. Mater. 162-164 (1984) 236.

[4] HINTON, F.L., CHU, M.S., Nucl. Fusion 25 (1985) 345.

[5] HINTON, F.L., Nucl. Fusion 25 (1985) 1457.

[6] HINTON, F.L., STAEBLER, G.M., Nucl. Fusion 29 (1989) 405.

[7] KOVANEN, M.A., CORE, W.G.F., HECTOR - A Code for the study of charged particles in axisymmetric tokamak plasmas, JET Joint Undertaking, JET-P(90)40, (1990), submitted for publication in J. Comput. Phys..

[8] STAMP, M.F., BEHRINGER, K.H., FORREST, M.J., MORGAN, P.P., SUMMERS, H.P., J. Nucl. Mater. 162-164 (1989) 404.

[9] REICHLE, R., SUMMERS, D.D.R., STAMP, M.F., 9th Int. Conf. on Plasma Surface Interactions, Bournemouth (1990), also to appear in J. Nucl. Mater.

[10] PEACOCK, A.T., COAD, J.P., LAMA, F., et al., 9th Int. Conf. on Plasma Surface Interactions, Bournemouth (1990), also to appear in J. Nucl. Mater.

[11] LAZZARO, E., MANTICA, P., Plasma Phys. and Contr. Fusion 30 (1988) 1735.

[12] O'BRIEN, D.P., KOVANEN, M.A., REICHLE, R., et al., Proc. 17th EPS Conf. on Controlled Fusion and Plasma Physics, Amsterdam (1990).

[13] KOVANEN, M.A., CORE, W.G.F., HELLSTEN, T., Finite orbit effects in ICRF heated tokamak plasmas, JET Joint Undertaking, JET-P(90)68, (1990), submitted for publication in Nucl. Fusion.

[14] STUBBERFIELD, P.M., WATKINS, M.L., JET Joint Undertaking, DPA(06)/87, (1987),

[15] WEISEN, H., BERGSAKER, H., CAMBELL, D., et al., Boundary ion temperatures in JET, submitted to Nucl. Fusion.

TABLE I

Mean energy of the particles hitting the inner and the outer strike zones in the upper X-point region; # 20998, t = 51.0 sec.

$T_i(\psi = 1.0)$ [keV]	$\langle E \rangle_{inner}$ [keV]	$\langle E \rangle_{outer}$ [keV]
0.10	0.08	0.11
0.25	0.24	0.20
1.00	1.16	0.80
1.50	1.58	1.13

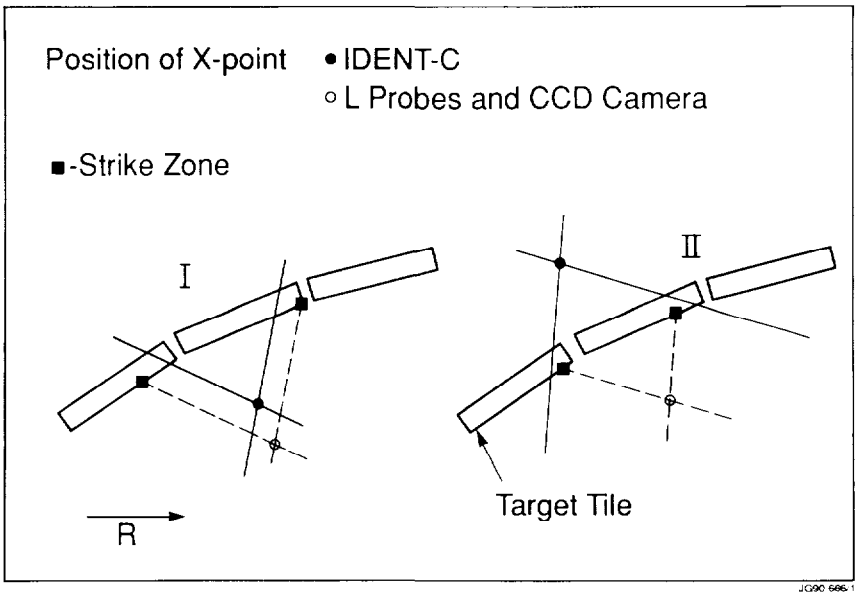

Fig. 1 X-point position as interpreted from CCD camera measurements compared with the calculated position from magnetic measurements with the IDENT-C code in two cases (I and II).

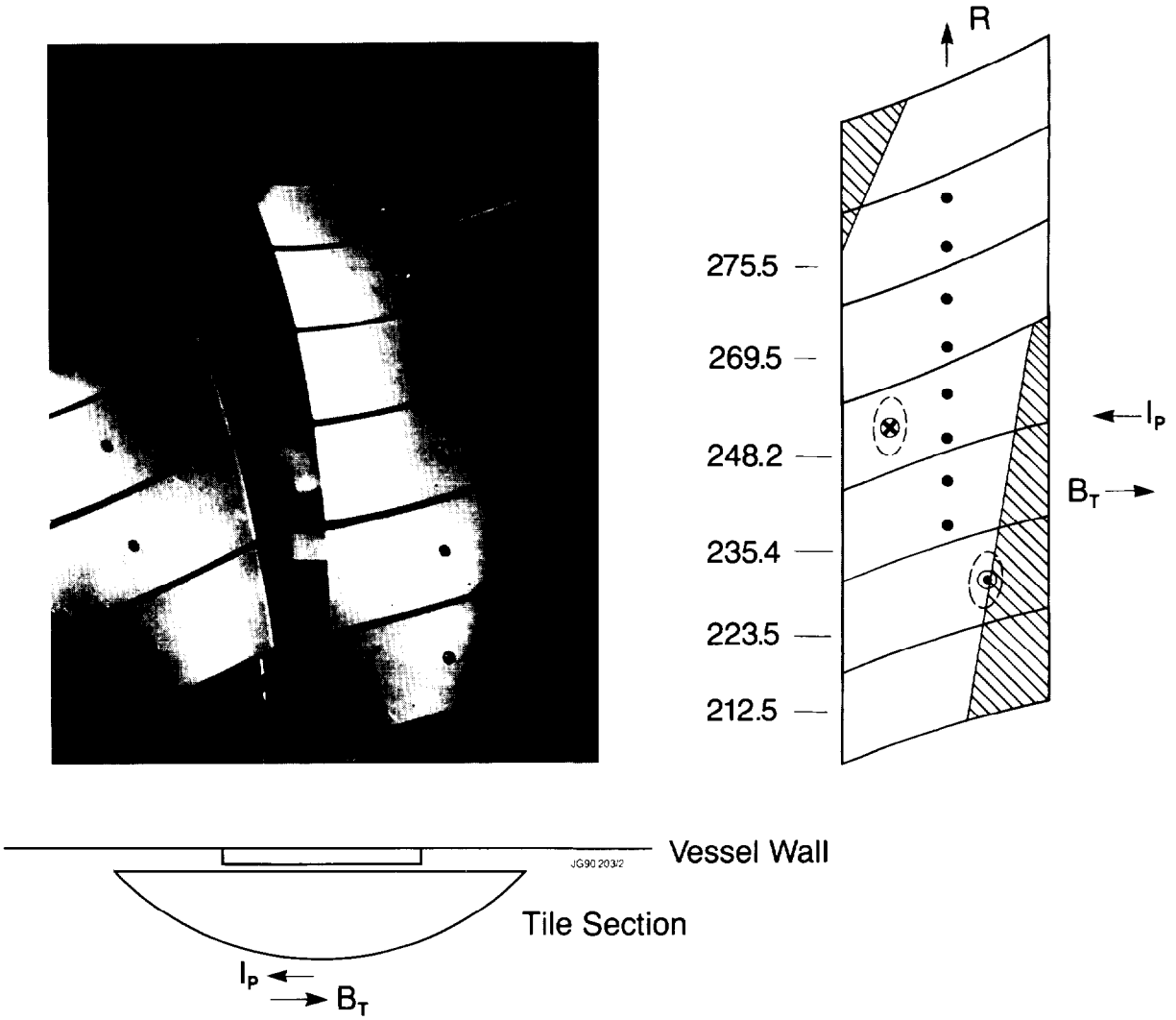

Fig. 2 View of the CCD cameras showing the toroidal curvature of the target tiles and a poloidal section with the ohmic strike zones.

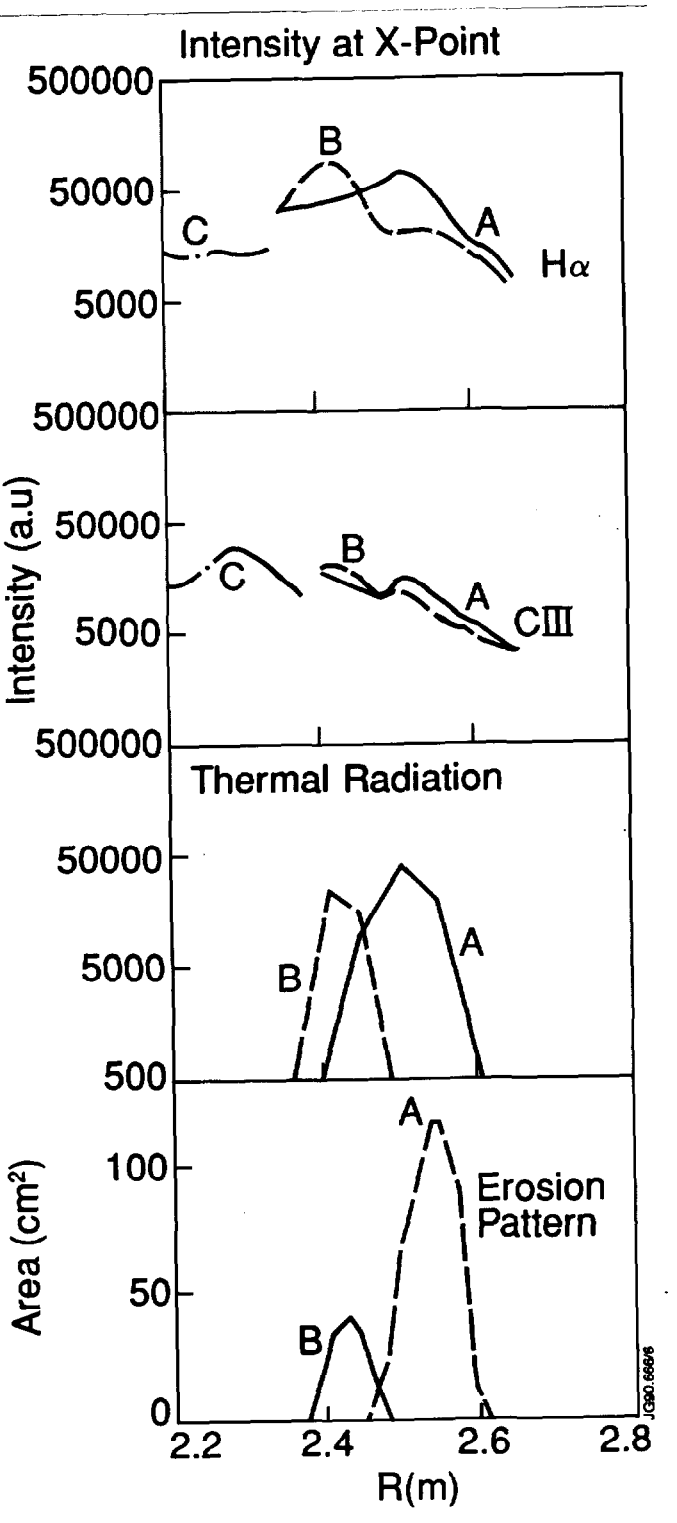

Fig. 3 Spatial correlation of H_α, C_{III} and thermal radiation for the strike zones A, B and C during the discharge 20995 compared with the erosion patterns.

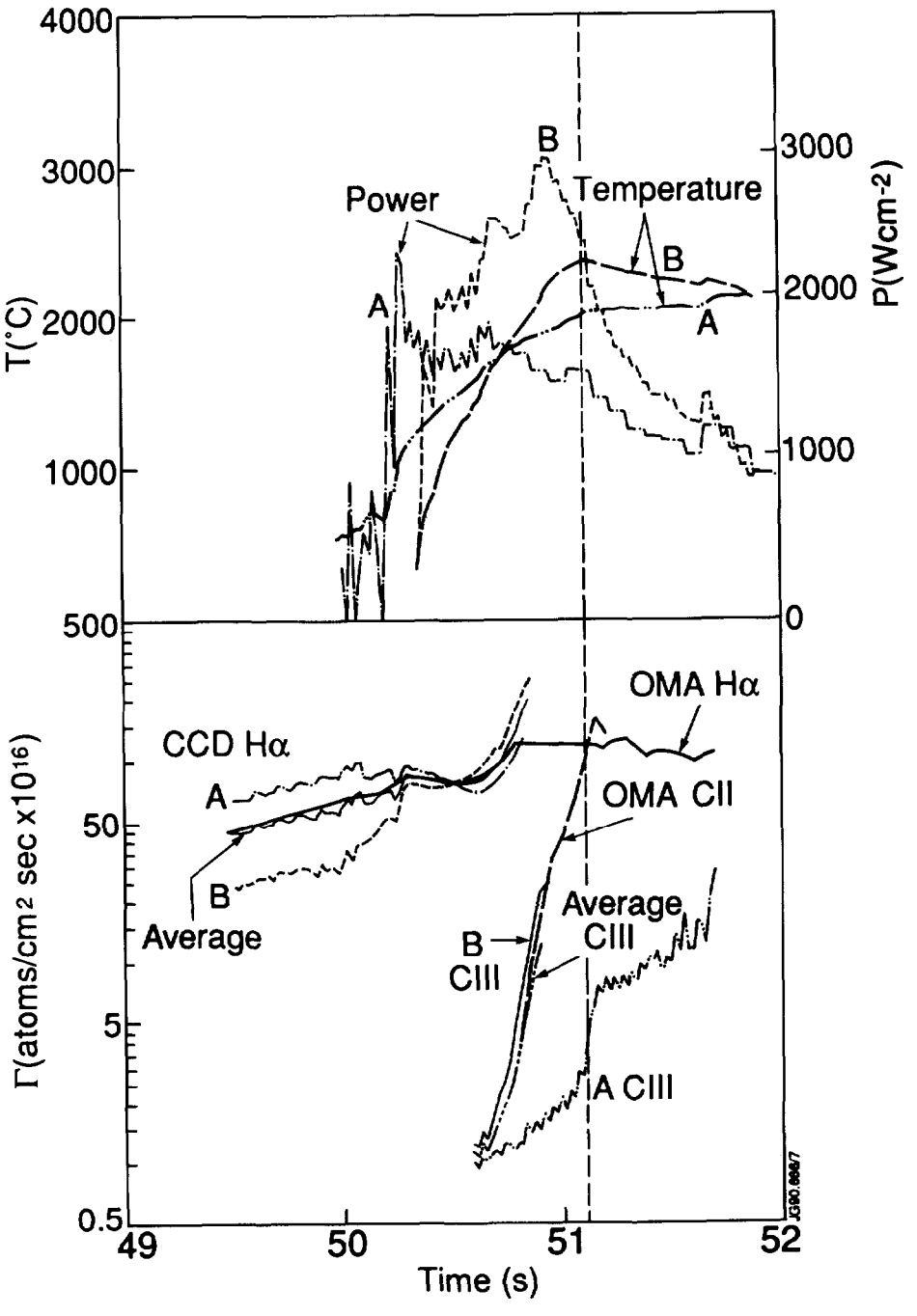

Fig. 4 Temporal development of temperatures, deposited power and particle fluxes in the strike zones A and B for the discharge 20995. The H_α signals are from discharge 21024. The carbon bloom is indicated at 51.1 sec.

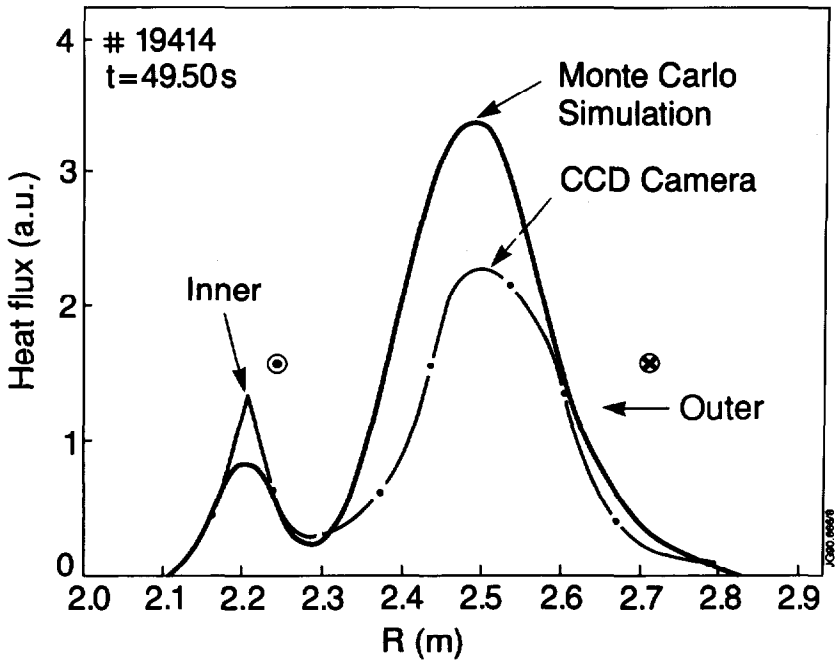

Fig. 5 Comparison of the heat flux intensity from Monte-Carlo simulation with that of the CCD cameras during an ohmic discharge.

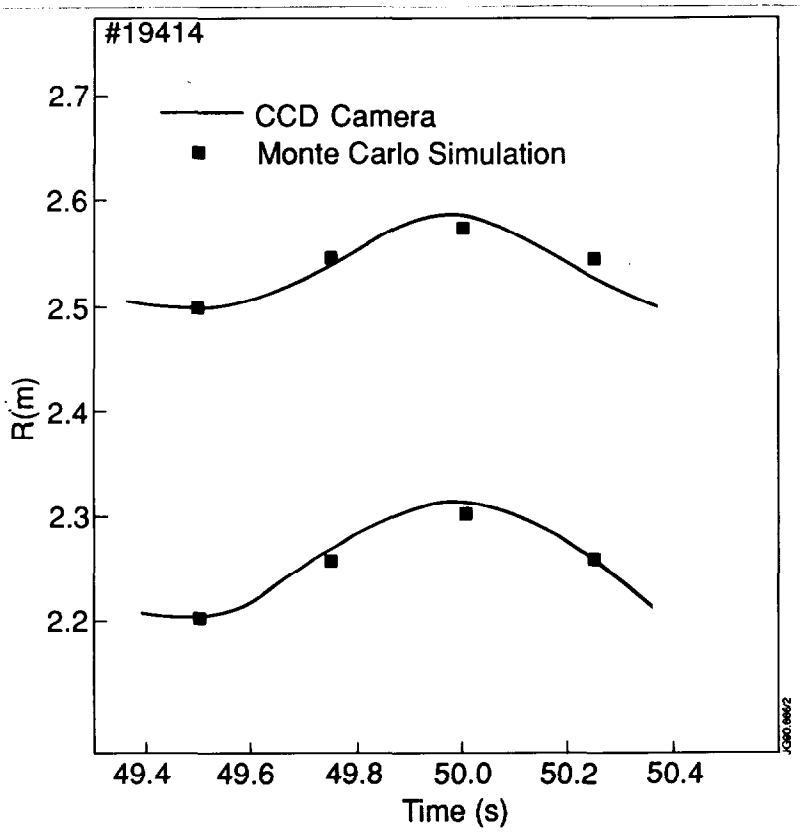

Fig. 6 The strike zone positions from the CCD cameras compared with the Monte-Carlo simulation during the horizontal sweep of the X-point.

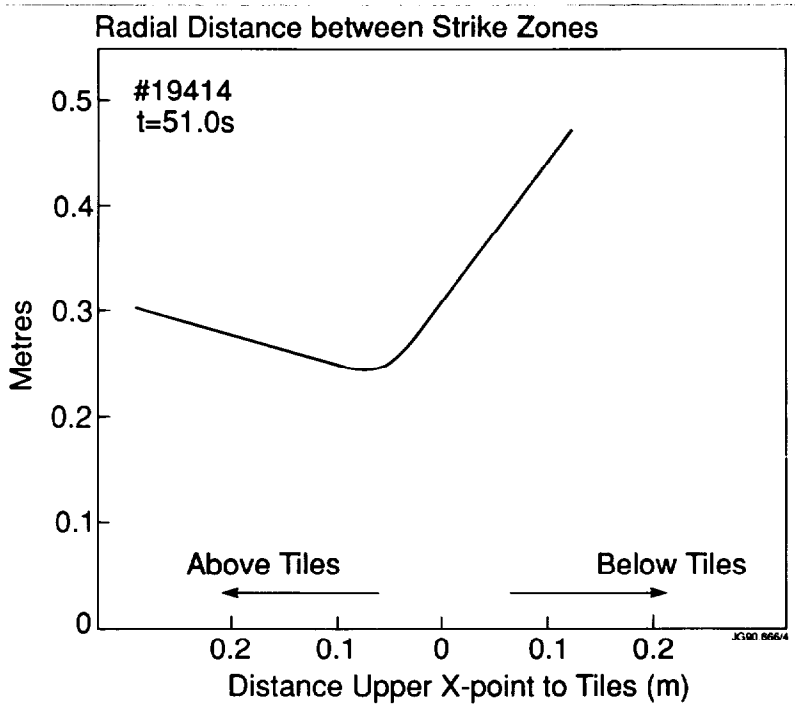

Fig. 7 Monte-Carlo simulation of the effect of the vertical X-point sweep. The position of the vessel wall was changed in a fixed magnetic field configuration.

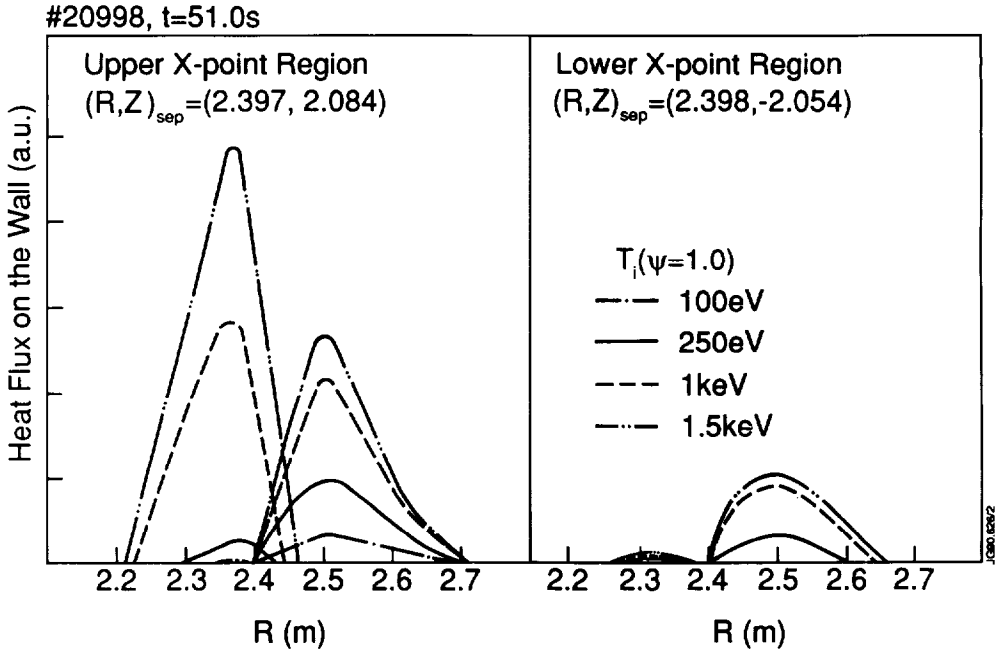

Fig. 8 Monte-Carlo simulation of the heat fluxes at the upper and lower X-point regions during the ion temperature scan. Other data for the discharge was kept unaltered during the scan.

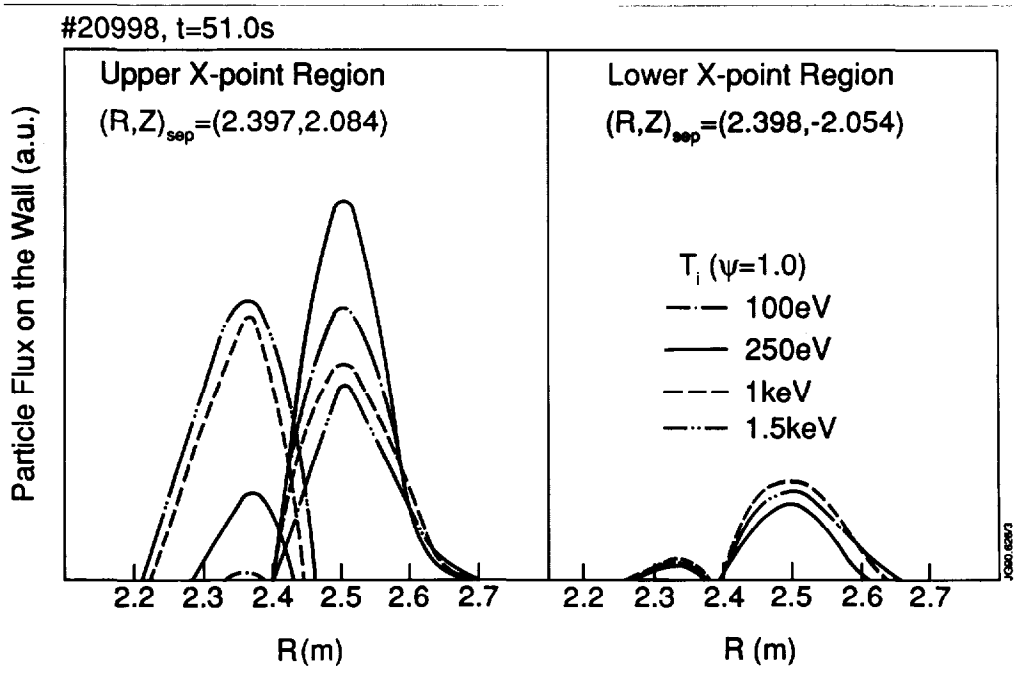

Fig. 9 Monte-Carlo simulation at the particle fluxes at the upper and lower X-point regions during the ion temperature scan. Other data for the discharge was kept unaltered during the scan.

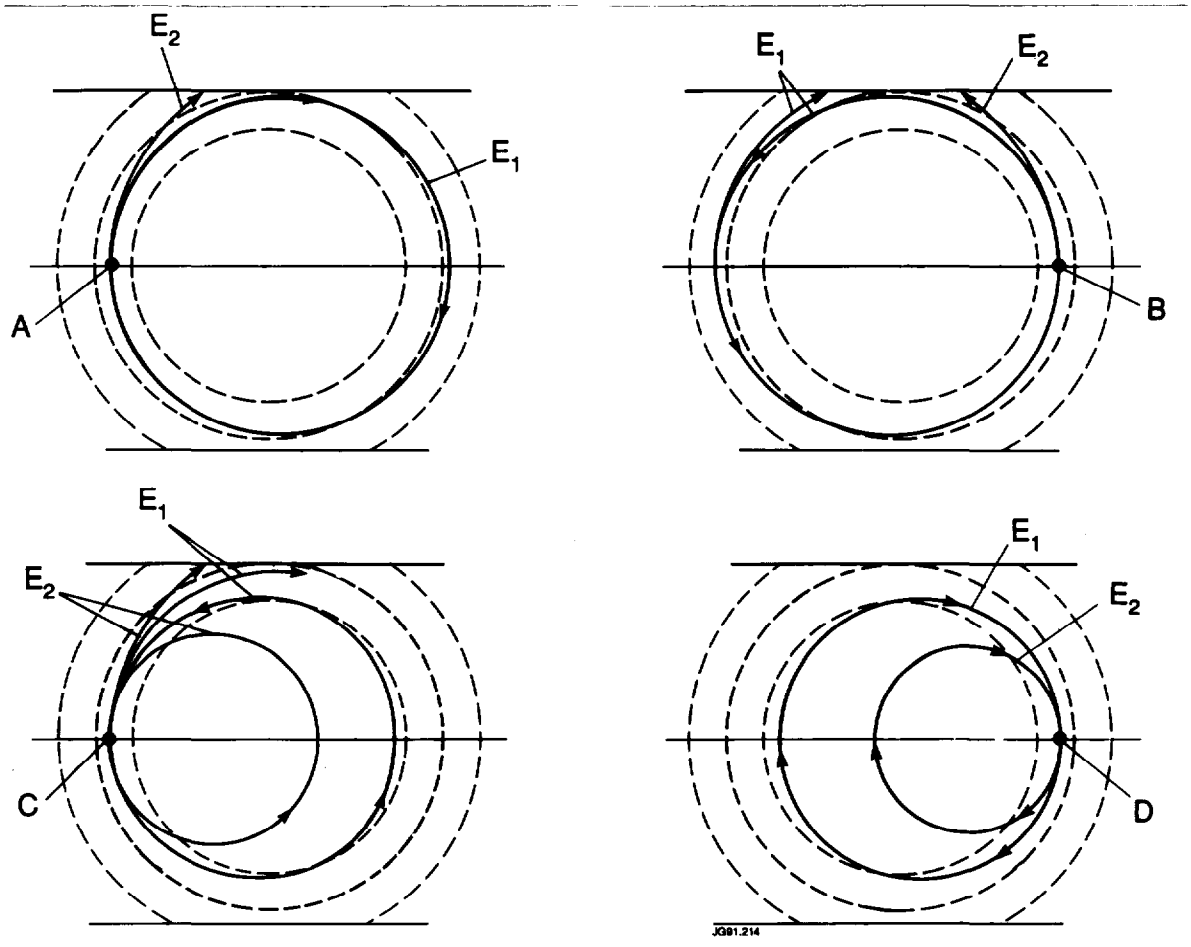

Fig. 10 Illustration of the orbit effects on the heat flux patterns due to increased plasma ion temperature. $E_1 < E_2$.

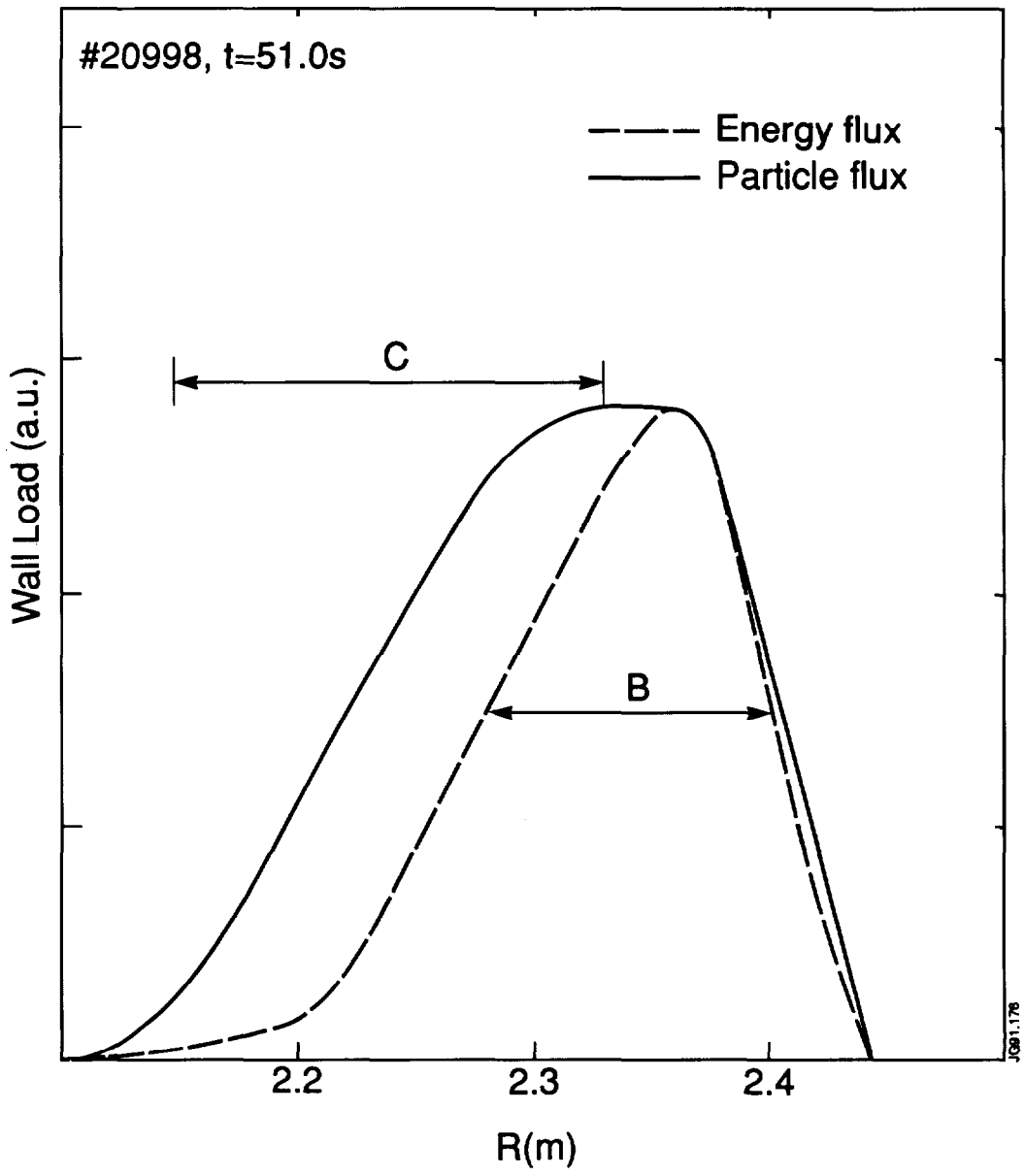

Fig. 11 Monte-Carlo simulation of the effect of the particle influx from the wall on the particle and heat fluxes in the X-point region. Strike zone C is produced with a source of low energy particles.

APPENDIX 1.

THE JET TEAM

JET Joint Undertaking, Abingdon, Oxon, OX14 3EA, U.K.

J.M.Adams[1], F.Alladio[4], H.Altmann, R.J.Anderson, G.Appruzzese, W.Bailey, B.Balet, D.V.Bartlett, L.R.Baylor[24], K.Behringer, A.C.Bell, P.Bertoldi, E.Bertolini, V.Bhatnagar, R.J.Bickerton, A.Boileau[3], T.Bonicelli, S.J.Booth, G.Bosia, M.Botman, D.Boyd[31], H.Brelen, H.Brinkschulte, M.Brusati, T.Budd, M.Bures, T.Businaro[4], H.Buttgereit, D.Cacaut, C.Caldwell-Nichols, D.J.Campbell, P.Card, J.Carwardine, G.Celentano, P.Chabert[27], C.D.Challis, A.Cheetham, J.Christiansen, C.Christodoulopoulos, P.Chuilon, R.Claesen, S.Clement[30], J.P.Coad, P.Colestock[6], S.Conroy[13], M.Cooke, S.Cooper, J.G.Cordey, W.Core, S.Corti, A.E.Costley, G.Cottrell, M.Cox[7], P.Cripwell[13], F.Crisanti[4], D.Cross, H.de Blank[16], J.de Haas[16], L.de Kock, E.Deksnis, G.B.Denne, G.Deschamps, G.Devillars, K.J.Dietz, J.Dobbing, S.E.Dorling, P.G.Doyle, D.F.Düchs, H.Duquenoy, A.Edwards, J.Ehrenberg[14], T.Elevant[12], W.Engelhardt, S.K.Erents[7], L.G.Eriksonn[5], M.Evrard[2], H.Falter, D.Flory, M.Forrest[7], C.Froger, K.Fullard, M.Gadeberg[11], A.Galetsas, R.Galvao[8], A.Gibson, R.D.Gill, A.Gondhalekar, C.Gordon, G.Gorini, C.Gormezano, N.A.Gottardi, C.Gowers, B.J.Green, F.S.Griph, M.Gryzinski[26], R.Haange, G.Hammett[6], W.Han[9], C.J.Hancock, P.J.Harbour, N.C.Hawkes[7], P.Haynes[7], T.Hellsten, J.L.Hemmerich, R.Hemsworth, R.F.Herzog, K.Hirsch[14], J.Hoekzema, W.A.Houlberg[24], J.How, M.Huart, A.Hubbard, T.P.Hughes[32], M.Hugon, M.Huguet, J.Jacquinot, O.N.Jarvis, T.C.Jernigan[24], E.Joffrin, E.M.Jones, L.P.D.F.Jones, T.T.C.Jones, J.Källne, A.Kaye, B.E.Keen, M.Keilhacker, G.J.Kelly, A.Khare[15], S.Knowlton, A.Konstantellos, M.Kovanen[21], P.Kupschus, P.Lallia, J.R.Last, L.Lauro-Taroni, M.Laux[33], K.Lawson[7], E.Lazzaro, M.Lennholm, X.Litaudon, P.Lomas, M.Lorentz-Gottardi[2], C.Lowry, G.Magyar, D.Maisonnier, M.Malacarne, V.Marchese, P.Massmann, L.McCarthy[28], G.McCracken[7], P.Mendonca, P.Meriguet, P.Micozzi[4], S.F.Mills, P.Millward, S.L.Milora[24], A.Moissonnier, P.L.Mondino, D.Moreau[17], P.Morgan, H.Morsi[14], G.Murphy, M.F.Nave, M.Newman, L.Nickesson, P.Nielsen, P.Noll, W.Obert, D.O'Brien, J.O'Rourke, M.G.Pacco-Düchs, M.Pain, S.Papastergiou, D.Pasini[20], M.Paume[27], N.Peacock[7], D.Pearson[13], F.Pegoraro, M.Pick, S.Pitcher[7], J.Plancoulaine, J-P.Poffé, F.Porcelli, R.Prentice, T.Raimondi, J.Ramette[17], J.M.Rax[27], C.Raymond, P-H.Rebut, J.Removille, F.Rimini, D.Robinson[7], A.Rolfe, R.T.Ross, L.Rossi, G.Rupprecht[14], R.Rushton, P.Rutter, H.C.Sack, G.Sadler, N.Salmon[13], H.Salzmann[14], A.Santagiustina, D.Schissel[25], P.H.Schild, M.Schmid, G.Schmidt[6], R.L.Shaw, A.Sibley, R.Simonini, J.Sips[16], P.Smeulders, J.Snipes, S.Sommers, L.Sonnerup, K.Sonnenberg, M.Stamp, P.Stangeby[19], D.Start, C.A.Steed, D.Stork, P.E.Stott, T.E.Stringer, D.Stubberfield, T.Sugie[18], D.Summers, H.Summers[20], J.Taboda-Duarte[22], J.Tagle[30], H.Tamnen, A.Tanga, A.Taroni, C.Tebaldi[23], A.Tesini, P.R.Thomas, E.Thompson, K.Thomsen[11], P.Trevalion, M.Tschudin, B.Tubbing, K.Uchino[29], E.Usselmann, H.van der Beken, M.von Hellermann, T.Wade, C.Walker, B.A.Wallander, M.Walravens, K.Walter, D.Ward, M.L.Watkins, J.Wesson, D.H.Wheeler, J.Wilks, U.Willen[12], D.Wilson, T.Winkel, C.Woodward, M.Wykes, I.D.Young, L.Zannelli, M.Zarnstorff[6], D.Zasche[14], J.W.Zwart.

PERMANENT ADDRESS

1. UKAEA, Harwell, Oxon. UK.
2. EUR-EB Association, LPP-ERM/KMS, B-1040 Brussels, Belgium.
3. Institute National des Récherches Scientifique, Quebec, Canada.
4. ENEA-CENTRO Di Frascati, I-00044 Frascati, Roma, Italy.
5. Chalmers University of Technology, Göteborg, Sweden.
6. Princeton Plasma Physics Laboratory, New Jersey, USA.
7. UKAEA Culham Laboratory, Abingdon, Oxon. UK.
8. Plasma Physics Laboratory, Space Research Institute, Sao José dos Campos, Brazil.
9. Institute of Mathematics, University of Oxford, UK.
10. CRPP/EPFL, 21 Avenue des Bains, CH-1007 Lausanne, Switzerland.
11. Risø National Laboratory, DK-4000 Roskilde, Denmark.
12. Swedish Energy Research Commission, S-10072 Stockholm, Sweden.
13. Imperial College of Science and Technology, University of London, UK.
14. Max Planck Institut für Plasmaphysik, D-8046 Garching bei München, FRG.
15. Institute for Plasma Research, Gandhinagar Bhat Gujat, India.
16. FOM Instituut voor Plasmafysica, 3430 Be Nieuwegein, The Netherlands.
17. Commissiariat à L'Energie Atomique, F-92260 Fontenay-aux-Roses, France.
18. JAERI, Tokai Research Establishment, Tokai-Mura, Naka-Gun, Japan.
19. Institute for Aerospace Studies, University of Toronto, Downsview, Ontario, Canada.
20. University of Strathclyde, Glasgow, G4 ONG, U.K.
21. Nuclear Engineering Laboratory, Lapeenranta University, Finland.
22. JNICT, Lisboa, Portugal.
23. Department of Mathematics, Univeristy of Bologna, Italy.
24. Oak Ridge National Laboratory, Oak Ridge, Tenn., USA.
25. G.A. Technologies, San Diego, California, USA.
26. Institute for Nuclear Studies, Swierk, Poland.
27. Commissiariat à l'Energie Atomique, Cadarache, France.
28. School of Physical Sciences, Flinders University of South Australia, South Australia SO42.
29. Kyushi University, Kasagu Fukuoka, Japan.
30. Centro de Investigaciones Energeticas Medioambientales y Techalogicas, Spain.
31. University of Maryland, College Park, Maryland, USA.
32. University of Essex, Colchester, UK.
33. Akademie de Wissenschaften, Berlin, DDR.

CR 88.49.1A